



# Diapycnal Mixing in Submesoscale Permitting Simulations of the Deep Brazil Basin

Yonglin Huang<sup>1</sup>, Annalisa Bracco<sup>2</sup>, Kurt Polzin<sup>3</sup>, and Jonanthan Gula<sup>4,5</sup>

<sup>1</sup>Georgia Institute of Technology, Atlanta, United States

<sup>2</sup>Euro-Mediterranean Center on Climate Change (CMCC), Milan, Italy

<sup>3</sup>Woods Hole Oceanographic Institution, Woods Hole, United States

<sup>4</sup>Université de Bretagne-Occidentale, CNRS, IRD, Ifremer, Laboratoire d’Océanographie Physique et Spatiale (LOPS), IUEM, Plouzané, France

<sup>5</sup>Institut Universitaire de France (IUF), Paris, France

**Correspondence:** Yonglin Huang (yhuang868@gatech.edu) and Annalisa Bracco (annalisa.bracco@cmcc.it)

**Abstract.** Modeling diapycnal mixing in the deep-ocean is challenging, particularly in regions with complex topography. Here we diagnose the relative roles of sub-inertial motions and tidal forcing focusing on the deep Brazil Basin in four simulations using a hydrostatic, high-resolution regional model (CROCO), at 1 km and 3 km horizontal resolution, in presence or absence of tides. Tracer particles are released at multiple depths to investigate the variability of modeled mixing estimates. In the model, horizontal resolution exerts the primary control on diapycnal mixing, while tidal forcing plays a secondary and resolution-dependent role. Increasing resolution significantly increases number and intensity of eddies and enhances diapycnal mixing across the water column. The comparison with the in-situ observations indicates that the simulated diffusivities near the bottom boundary layer are comparable in value to observational estimates. However, diffusivities in the stratified interior are overestimated due to bathymetric smoothing, which causes an underestimation of high-mode internal tides and allows eddy-driven motions to dominate.

## 1 Introduction

In the ocean, diapycnal mixing governs the vertical exchange of mass, heat, salt, and tracers across density surfaces, thereby controlling ocean stratification. Through irreversible turbulent fluxes, diapycnal mixing provides also the mechanical energy dissipation required to sustain the upwelling branch of the overturning circulation (Ferrari et al., 2016; Polzin and McDougall, 2022). Although background mixing rates in the ocean interior are weak, observations consistently show that strongly localized enhancements near rough topography dominate the net diapycnal transport and water mass transformation (Polzin et al., 1997; Ledwell et al., 2000). Multiple mechanisms contribute to topographically enhanced mixing, including internal hydraulic jumps (Legg and Klymak, 2008), Ekman layer processes (Garrett et al., 1993), internal wave generation and breaking (Wunsch and Ferrari, 2004), vertically sheared layered vortices (Mashayek et al., 2024), and overturning instabilities (McWilliams, 2016).

The efficiency of topographic mixing depends sensitively on regional circulation and bathymetric detail, and thus, in ocean models, on model resolution. While increasing computational power now permits global and basin scale simulations



at mesoscale-resolving and even submesoscale-permitting resolution, these models often produce counterintuitive diapycnal mixing relative to coarser configurations, largely because they retain vertical mixing parameterizations developed for much lower resolution systems (Chen et al., 2025). Here, we compare submesoscale-permitting and mesoscale-resolving simulations performed with a widely used ocean model to quantify how modeled diapycnal diffusivities and the underlying mixing processes depend on resolution in the Brazil Basin (BB). This region is particularly well suited for such an analysis, as it hosted the Brazil Basin Tracer Release Experiment (BBTRE), one of the first efforts to directly observe turbulent diapycnal mixing near fracture zones as part of the World Ocean Circulation Experiment. Understanding this dependence is key to the development of next generation ocean models, whether based on explicit turbulence resolving dynamics or emerging machine learning and AI based parameterizations (e.g., Zanna and Bolton (2020); Dheeshjith et al. (2025)).

In summary, our analysis focuses on evaluating whether hydrostatic, terrain-following, mesoscale resolving or submesoscale permitting models realistically represent near-bottom diapycnal mixing over rough topography, and on identifying strengths and limitations across resolutions. The Brazil Basin offers a well-constrained testbed for this work due to its distinctive bathymetry and the availability of historical observations, allowing us to assess the relative roles of submesoscale circulations and tidal and wave-driven motions in shaping bottom boundary layer dynamics.

## 2 Materials and Methods

### 2.1 Regional Context and Numerical Model

The study region, which is shown in Fig. 1a, covers a portion of the Brazil Basin occupied in 1997 by the BBTRE. The abyssal circulation is dominated by Antarctic Bottom Water (AABW) which flows northward and enters the Brazil Basin from the Southern Ocean through the Vema and Hunter channels.

The circulation of the Brazil Basin is simulated by the Coastal and Regional Ocean Community (CROCO) model (Auclair et al., 2024), built upon the Regional Ocean Modeling System (ROMS) (Shchepetkin and McWilliams, 2005). CROCO solves the free surface, hydrostatic primitive equations and adopts terrain-following vertical coordinates. Despite the limitations inherent to the hydrostatic assumption, the model configuration adopted here reflects the prevailing framework of state-of-the-art ocean and climate models.

We analyze the GIGATL simulations (Gula et al., 2021), a set of ocean-only high-resolution runs performed over the Atlantic Ocean. We focus on four simulations, at 1 km (GIGATL1) and 3 km (GIGATL3) horizontal resolution, with 100 vertical levels, with (GIGATL1T/GIGATL3T) and without (GIGATL1N/GIGATL3N) tides and analyze the common period of July 2009 using hourly averaged model outputs. In all cases, hourly momentum and heat fluxes from the Climate Forecast System Reanalysis (CFSR) (Saha et al., 2010) force CROCO using a bulk formulation and a stress correction, while initial and boundary conditions are supplied by the Simple Ocean Data Assimilation (SODA) reanalysis (Carton and Giese, 2008). The barotropic tidal forcing at the boundaries and tidal potential in the tidal runs is derived from TPXO7.2 and GOT99 (Ray, 1999).

All configurations adopt a third-order upwind scheme (UP3) and its rotated split variant RSUP3 for momentum and tracers to reduce dispersive ringing and keep transport bounded while helping preserve fronts and filaments within the resolution

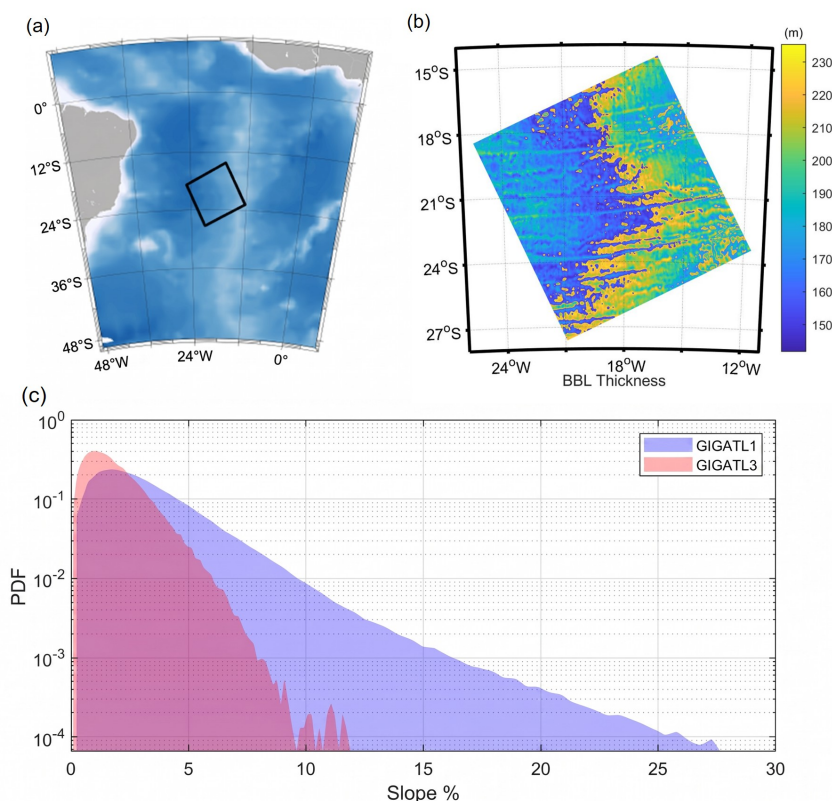


**Figure 1.** Study region and context in the abyssal Brazil Basin. (a) Map of the Brazil Basin showing the model study region (black box). (b) Bottom boundary layer (BBL) thickness in the GIGATL simulations. (c) Probability density function of slope distribution of GIGATL1 (1 km resolution) and GIGATL3 (3 km resolution) simulations in the black box.

55 limits. In the vertical, SPLINES are used for both momentum and tracers. The conservative parabolic–spline reconstruction provides high–order accuracy for steep vertical gradients to limit numerical mixing while maintaining stability. Explicit lateral diffusivity is not included, and vertical mixing is parameterized with the k-epsilon turbulence closure scheme with the Canuto A-stability function (Umlauf and Burchard, 2003). Bottom friction is parameterized using a logarithmic law of the wall incorporating a roughness length of 0.01 m. The bathymetry is interpolated from the SRTM30plus dataset (NASA Shuttle Radar  
60 Topography Mission, 2013) and then smoothed with a Gaussian kernel to prevent the steepness of the topography from exceeding  $r_{max}=\Delta H/H=0.2$  ( $H$  is bottom depth [m] and  $\Delta H$  is topography increment). The distribution of terrain-following s-levels is set by the surface and bottom stretching parameters  $\theta_s, \theta_b$  that control vertical grid refinement near the surface and seafloor with larger values clustering more levels in the respective boundary layers. The reader is referred to Song and Haidvogel (1994)  
65 constraints, only topographic features at an “effective resolution” scale of 2.5 km for the GIGATL1 runs and 7.5 km for the



GIGATL3 cases are well resolved, while smaller features are increasingly smoothed (Fig. 1c). The Brazil Basin, however, is characterized by abyssal hills that have a typical distance between peaks of 6-8 kilometers and present conditions with critical to near-critical topographic slopes with regards to internal tidal motions. The region's distinctive bathymetry includes canyons spanning 10–100 km and smaller abyssal hills with scales of 1–10 km. More details of the GIGATL runs and comparisons with observations over the Atlantic basin can be found in Qu et al. (2021); Tagliabue et al. (2022); Vic et al. (2022); Schubert et al. (2025).

### 2.1.1 BBL Definition

Focusing on the BBL, Fig. 1b shows its modeled thickness in the region of interest, a quantity that we will use later in this work. The thickness was determined using a density threshold with its upper boundary coinciding with a change in density of  $0.001 \text{ kg/m}^3$  from the deepest grid point in the model. Assuming a background stratification of  $1 \times 10^{-6} \text{ s}^{-2}$ , the BBL typically ranges from  $O(10)$  to  $O(100)$  m. However, over steep slopes, especially near the mid-ocean ridge, the BBL thickness can surpass 200 m, reflecting strong abyssal water transformation. The BBL thickness is insensitive to resolution or tidal forcing and is nearly identical across all simulations.

### 2.1.2 Energy Conversion Rates

To quantify whether the mean flow field energizes mesoscale or submesoscale variability, we diagnosed the barotropic (BTC) and baroclinic conversion (BCC) terms. Following Brum et al. (2023), BTC and BCC terms were calculated on the fixed-depth surface  $z = -4000$  m as follows:

$$\text{BTC} = -\rho_0 \left[ \langle u'^2 \rangle \frac{\partial \bar{u}}{\partial x} + \langle u'v' \rangle \frac{\partial \bar{u}}{\partial y} + \langle u'v' \rangle \frac{\partial \bar{v}}{\partial x} + \langle v'^2 \rangle \frac{\partial \bar{v}}{\partial y} \right] \quad (1)$$

$$\text{BCC} = -\frac{g^2}{\rho_0 N^2} \left( \langle \rho' u' \rangle \frac{\partial \bar{\rho}}{\partial x} + \langle \rho' v' \rangle \frac{\partial \bar{\rho}}{\partial y} \right) \quad (2)$$

Here,  $\rho_0$  is a reference density.  $\bar{u}$  and  $\bar{v}$  are the mean horizontal velocities with overbars denoting monthly means at each grid point.  $u'$  and  $v'$  are deviations from those means, and  $\bar{\rho}$  is the mean density,  $\rho'$  is the density anomaly, and  $N^2$  is the local buoyancy frequency.

BTC quantifies the rate at which Reynolds stresses act against the horizontal shear of the mean flow and thus measures the transfer of mean kinetic energy into eddy kinetic energy (EKE). Positive BTC is a signature of barotropic instability or shear production of EKE. BCC measures the transfer between mean potential and eddy potential energy (EPE). Positive BCC is indicative of downgradient horizontal eddy density fluxes, and therefore consistent with baroclinic instability.



### 2.1.3 Tracer Particles Tracking

To evaluate the modelled mixing, we performed offline Lagrangian particle tracking simulations with Ichthyop, an open-source Java-based Lagrangian model designed for particle simulations in  $\sigma$ -coordinate models like CROCO. Ichthyop reads the time-varying CROCO velocity fields and then advects virtual particles according to:

$$\frac{d\mathbf{x}}{dt} = \mathbf{v}(\mathbf{x}, t) \quad (3)$$

where the vector  $\mathbf{x} = \mathbf{x}(x, y, z)$  represents the position of the particles, and  $\mathbf{v}$  represents the three-dimensional Eulerian velocity at the location and time.

We released strictly passive particles, with no explicit diffusion or random walk component added, ensuring the diffusivity estimates reflect mixing in CROCO (both numerical and parameterized mixing). We released in each simulation five clouds of 10,000 tracer particles around the BBTRE site (all over the black box in Fig. 2), one every two days during 1–11 July, 2009, at three depths, in the bottom-most model layer (about 40 m above the seafloor), at 3000 m and at 4000 m. The initial standard deviation of the vertical spread of tracer ( $\sigma_0$ ) was set to 9 m, as measured in the BBTRE. Each particle was tracked for 20 days.

Clouds of particles were also released in the annular region between 1.2 and 3 eddy radii of the surrounding coherent eddies, as well as in the background flow between eddies. Examples of the release strategy is provided in Fig. A1.

### 2.1.4 Estimated Diffusivity

Diapycnal (vertical) diffusivity  $K$  was diagnosed with two complementary methods: (i)  $K_z$  obtained from a tracer–moment estimate based on the density variance of the spread of tracer particles, and (ii)  $K_{BBL}$  obtained as a layer-mean estimate of diapycnal diffusivity within the BBL.

$K_z$  is obtained from the spreading rate of the particles in the density field following the tracer-moment method described in Ruan and Ferrari (2021). More specifically,  $K_z$  is obtained as

$$K_z = \frac{1}{2} \frac{d}{dt} \left[ \frac{\langle (\rho - \langle \rho \rangle)^2 \rangle}{|\nabla \rho|^2} \right] \quad (4)$$

where  $\rho$  is density, and  $\nabla \rho$  is the local density gradient. This formulation relates the growth of tracer variance to diffusivity, but is generalized to stratified flows by considering tracer moments in buoyancy coordinates. To avoid biasing the estimate of vertical diffusivity by combining particles sampling different stratification regimes, the initial particle release region was partitioned into multiple three-dimensional bins in longitude, latitude, and depth. Within each bin, diapycnal diffusivity was estimated from the trajectories of particles released in that bin. The resulting estimates were then combined using particle-number weighting to obtain the domain-integrated  $K_z$ .



For a more direct comparison with the BBTRE data, in the case of the release right atop the BBL, we also considered  
120 an inverse model that removes the spatial and temporal variations from the background field following Ledwell (2024) and  
according to:

$$K_{\text{BBL}} = \frac{UH \left( \frac{d\rho_{\text{BBL}}}{dx} \right)}{\frac{\partial \rho_{\text{BBL}}}{\partial z}} \quad (5)$$

where  $U$  is the mean flow lateral velocity over the releasement region during the trajectories and  $H$  is the bottom boundary  
layer thickness, assumed to be constant in space, and  $\rho_{\text{BBL}}$  is the density at the top of the BBL.

## 125 3 Results

### 3.1 The simulated flow field

From an observational perspective, the near surface circulation of the Brazil Basin is characterized by a weak sub-inertial flow  
(i.e. eddies), while the deep waters dynamics are thought to be controlled by inertial motions induced by the interaction of  
the flow with the topography (Polzin, 2009). In the CROCO simulations, the upper layers confirm low levels of eddy kinetic  
130 energy compared to other areas of the Atlantic, while the modeled BBL is occupied by incoherent vorticity perturbations  
and numerous, but short lasting, submesoscale eddies and vorticity filaments. The absence of major mesoscale systems in the  
BBL agrees with the low eddy kinetic energy levels measured in the Deep Basin Experiment. The near-bottom mean currents  
(Fig. A2), however, have amplitudes generally larger than observed values, potentially as a consequence of a pressure error.  
Above the BBL, many mesoscale and submesoscale eddies populate the vorticity field in all simulations, and they are more  
135 abundant and intense in the GIGATL1 runs, where are characterized by a local  $R_o \sim 1$  and often surrounded by a ring of  
intense, opposite-signed relative vorticity (Fig. 2c-f). The generation of a rich deep eddy field is independent of the vertical  
discretization choice, and was already noted in simulations of the same region using the MITgcm ocean model in its hydrostatic  
configuration, albeit in a less realistic setup (Drake et al., 2022b).

At 3000 m depth, vorticity snapshots reveal energetic anticyclonic and cyclonic eddies with a preference for the formers.  
140 They have size close to the baroclinic Rossby radius of deformation ( $\sim 50$  km) and extend to about 2000 m (Fig. 2e-f). The eddy  
generation occurs in all simulations, independently of tidal presence (Fig. A3), and the eddies are characterized by enhanced  
vertical velocities at their periphery (Fig. 2g-h).

The marked difference in eddy coherence in and above the BBL suggests differing energy cascade dynamics near the bottom  
versus the interior ocean. Bottom interactions prevent the formation of mesoscale structures, while in the interior such formation  
145 is promoted. Both barotropic and baroclinic processes are at play according to the energy conversion analysis (Fig. 3a-d).

The formation of mesoscale eddies locally enhances the EKE of the flow via buoyancy fluxes and consequently mixing, as  
suggested by  $\overline{\omega' b'}$  shown in Fig. 3e-f.  $\omega'$  and  $b'$  are the vertical velocity and buoyancy perturbations to the monthly-averaged

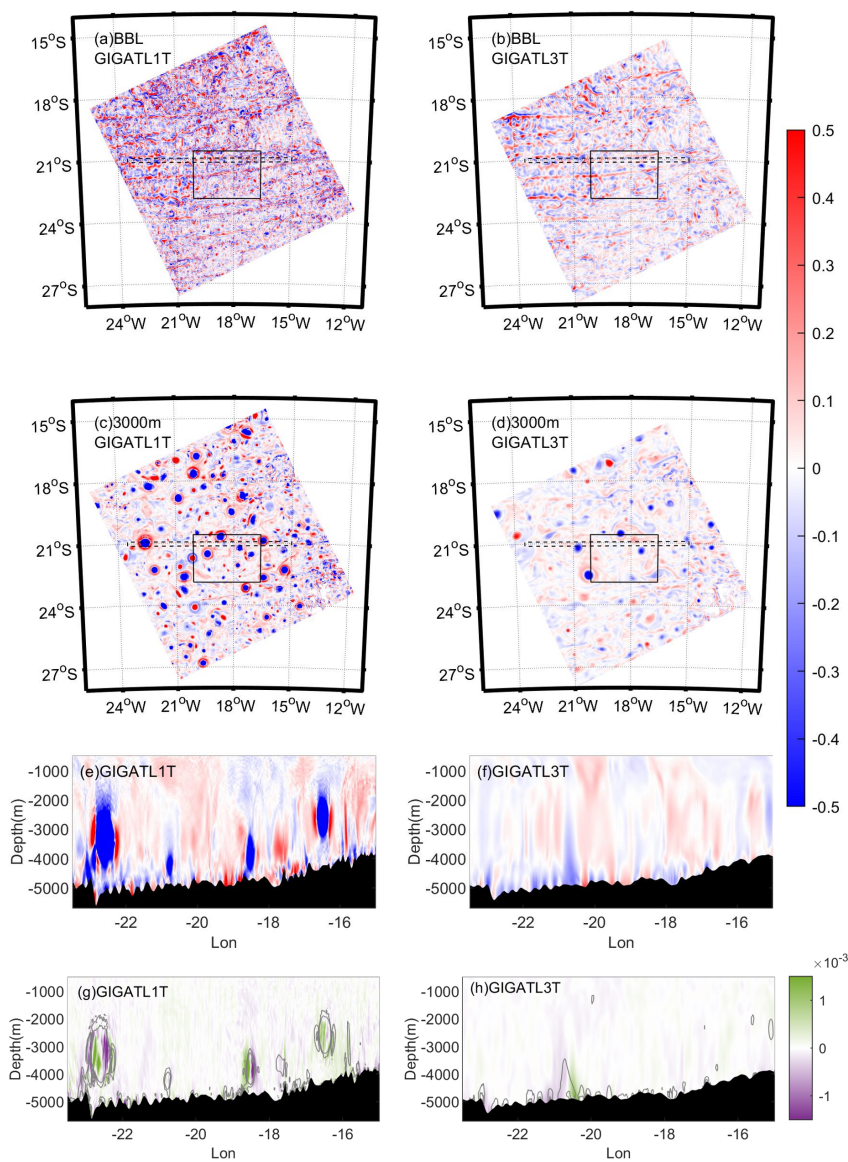


**Figure 2.** 5-day averaged vorticity field in GIGATL1T (a,c), GIGATL3T (b,d) at the top of BBL (a,b) and at 3000 m (c,d); vorticity profiles along 21°S (dash square in a-d) in the GIGATL1T (e) and GIGATL3T (f) simulations. Vertical velocity across the same transect in GIGATL1T (g) and GIGATL3T (h). Contour lines represent vertical vorticity normalized by the Coriolis parameter ( $\zeta/f$ ), with specified levels at -0.5, -0.25, 0.25, and 0.5 in the GIGATL1T cases (g), and at -0.25, -0.125, 0.125, and 0.25 in the GIGATL3T simulations (h).

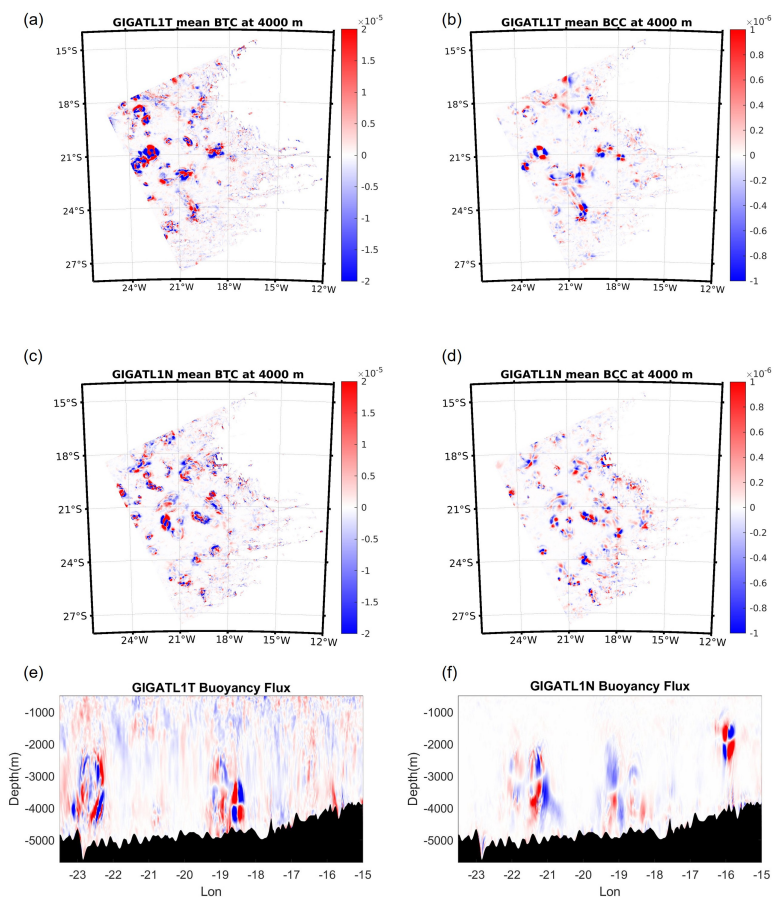


**Figure 3.** Monthly mean of BTC ( $\text{W m}^{-1}$ ) (a,c) and BCC ( $\text{W m}^{-1}$ ) (b,d) at the depth of 4000m in GIGATL1T and GIGATL1N. Profiles of 5-days averaged buoyancy flux along  $21^\circ\text{S}$  in (e) GIGATL1T and (f) GIGATL1N.

background flow (Gula et al., 2022). Enhanced vertical covariance can be found inside and around the eddies in the GIGATL1 simulations, independently of the tidal presence, while it is much weaker in the GIGATL3 runs (Fig. A4) where the eddies are less intense. In the background flow between the eddies, on the other hand, only the tidal presence supports buoyancy exchanges, in both GIGATL1T (Fig. 3) and GIGATL3T simulations (Fig. A4).

### 3.2 Lagrangian Tracer Particles Release Experiment

Next, we quantify how the differences in the flow field (stronger/weaker eddies and presence/absence of tidal-induced buoyancy exchanges) translate in different representations of vertical transport and mixing across the four simulations.



155 The particle vertical displacement in density space and dispersion  $A^2$ , quantified as  $A^2(t; t_0) = \frac{1}{N} \sum_{i=1}^N |x(t) - x(t_0)|^2$ , where  $N$  represents the total number of particles released in the targeted region,  $x(t)$  denotes the position of the  $i$ -th particle at time  $t$  and  $t_0$  is the initial release time, are shown in Fig. A5.

In the BBL, the vertical dispersion follows a ballistic regime for about one day, then the curves display slopes ranging from  $A^2 \sim t^{0.75}$  to  $A^2 \sim t^1$ . In this regime (day 2 to day 20), the vertical dispersion is greater in the GIGATL1 runs than in the GIGATL3 simulations, as found in analogous comparisons at the ocean surface (Zhong and Bracco, 2013). Tidal motions play a lesser role compared to model resolution, with the vertical dispersion in the tidal integrations slightly exceeding that of the no-tide cases in the GIGATL3 runs and being nearly indistinguishable after the first day in the GIGATL1 simulations, especially at the bottom layer. Higher in the water column, at 3000 m, the slopes of the dispersion curves are around 0.5-0.7 in the tidal runs, suggesting that eddies may modulate vertical dispersion (Callies, 2018; Drake et al., 2022a; Yankovsky et al., 2022). In the water column, the presence of tides has a greater impact than in the BBL.

In terms of displacement, particles in the GIGATL1 runs form thin filaments while maintaining an approximately Gaussian overall distribution, and they spread more thoroughly than in GIGATL3. Displacement is also slightly greater when tides are included. The inclusion of tides intensifies vertical velocities and increases vertical displacement, but the enhancement in tidal simulations remains secondary to the resolution effect. The enhancement is greater in the GIGATL3 case than in the GIGATL1 simulations.

### 3.3 Estimated Diffusivity

Next, we diagnose the vertical diapycnal diffusivity, and compare it to the values obtained from the BBTRE.

The vertical structure of  $K_z$  in both GIGATL1 and GIGATL3 is shown in Fig. 4. The modeled diapycnal diffusivity is enhanced toward the bottom and decreases moving away from it, which is consistent with the BBTRE measurements. Independently of the definitions used, diffusivity is higher in the GIGATL1 runs than in the lower resolution cases. As anticipated by the energetic analysis,  $K_z$  increases with horizontal resolution, and tidal motions impacts  $K_z$  in GIGATL1 more so than in GIGATL3 at all depths.

Comparing our modeled diapycnal diffusivity with observational estimates in the Brazil Basin is complicated by the different vertical resolution of the model compared to the in-situ measurements, and by differences in spatial coverage between observed dye and modeled tracers. Nonetheless, the GIGATL1 simulations compare well to published observed values atop the BBL. Field measurements in BBTRE showed diffusivities of  $2 - 4 \times 10^{-4} \text{ m s}^{-2}$  at about 500 m above an abyssal hill (Ledwell et al., 2000), increasing to over  $10^{-3} \text{ m s}^{-2}$  in the BBL, and the GIGATL1 simulations show very good agreement, with a slight underestimation for GIGATL3. Above the BBL, at 4000 m depth, however, only the GIGATL3 and GIGATL1N values are within the observed values considering uncertainties, while the diffusivity in GIGATL1T overestimates the observations. Higher up in the water column, the modeled diffusivities overestimate the observational values in all runs, with a larger bias in the GIGATL1T case. Overall, mixing does not decline with height in the simulations as sharply as it does in the observations.

The energy conversions and vertical dispersion analysis points to eddies as key players in modulating the modeled diapycnal diffusivity, with tides contributing only to the diffusivity of the background field. To further quantify the contribution of the

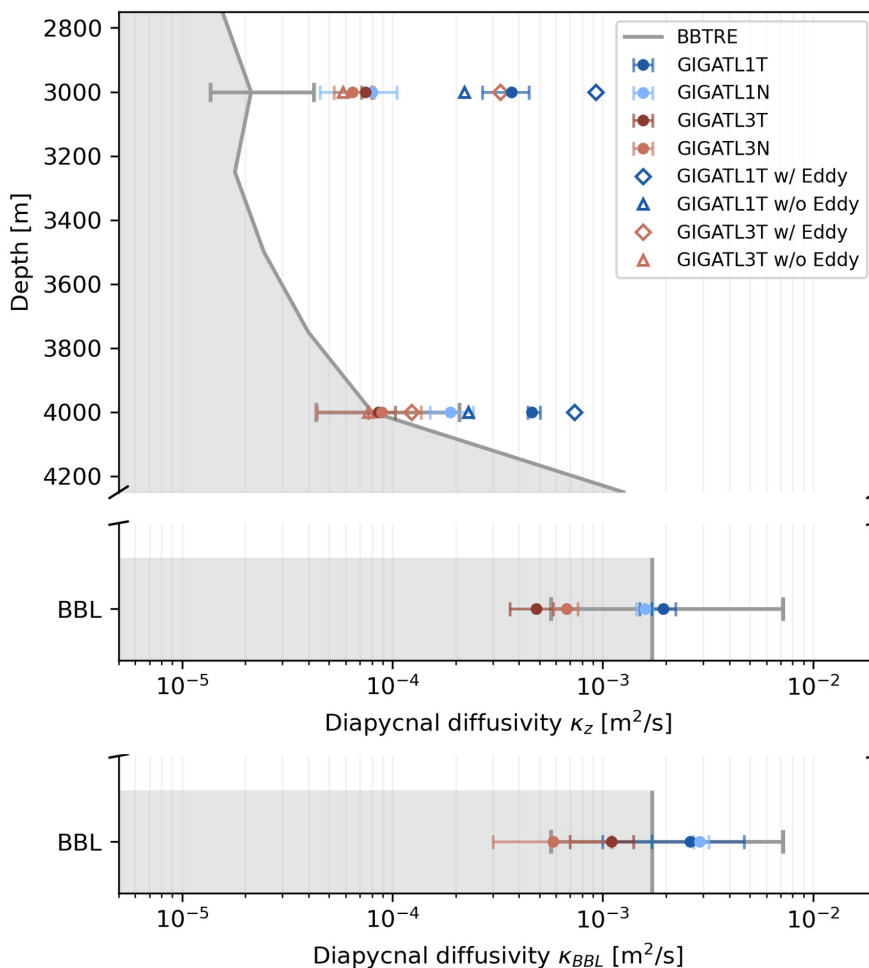


**Figure 4.** Diffusivities in the abyssal Brazil Basin in the observations and the four GIGATL simulations: vertical diapycnal diffusivity  $K_z$ , and BBL diffusivity  $K_{BBL}$ . Gray shading and lines represent BBTRE observations. Horizontal bars indicate ranges (max-min) across sampled patches and the depths at which tracer particles were released in the CROCO simulations. Values from releases around eddies or in the background flow at 3000 and 4000 m depth are also indicated.



eddies to the interior diffusivity, we conducted several sensitivity experiments by altering the tracer release locations. Narrow-  
190 ing the tracer release to only eddies or background areas, including a release at the exact location of BBTRE (21.7°S, 18.3°W)  
changes our modeled estimates. Whenever the tracers are placed in the background around the coherent eddies, they undergo  
smaller amount of diapycnal mixing. Vice versa, mixing is enhanced (about 2-4 times as much as in the background in the  
GIGATL3 case and more than three times larger in the GIGATL1 simulations) in and especially around the eddy cores.

Last, we compare our  $K$  estimates with prior modeling studies. Using the MITgcm configured in a semi-idealized domain  
195 resembling the BBTRE release location at 600 m horizontal resolution, Drake et al. (2022b) estimated  $K_z$  near the bottom using  
Eq. 4 modified to account only for temperature. They found a diffusivity value of about  $1.50 \times 10^{-3} \text{ m s}^{-2}$  at day 25 from the  
release of the tracers, which is broadly consistent with our GIGATL1 values. Moving to other regions, Mashayek et al. (2024)  
investigated the enhancement in BBL turbulence induced by shear and submesoscale instabilities in seamount wakes. They  
focused on the New England Seamounts in the North Atlantic and estimated the diapycnal diffusivity to exceed  $1 \times 10^{-3} \text{ m s}^{-2}$   
200 within a few hundred meters over the seafloor, especially around wake vortices as a result of an active submesoscale field.  
Similar values were captured by submesoscale permitting simulations of the Gulf of Mexico (Bracco et al., 2016), and in  
agreement with tracer release observations at the same location (Ledwell et al., 2016).

#### 4 The realism of the modeled world: Bathymetric smoothing and the modeled eddy field

In the simulations, diapycnal mixing is modulated by the eddy field, with tides having a secondary role and not impacting  
205 the evolution of the eddy field whenever the Rossby deformation radius of the BBL is resolved (Fig. 2 & A3). However, both  
theory (e.g., Munk and Wunsch (1998)) and observations (e.g., Polzin et al. (1997); Ledwell et al. (2000) identify internal  
waves generated by tide-topography interactions as the primary driver of diapycnal mixing in the deep ocean in regions of  
steep topography. Whenever the internal wave trajectories parallel the topographic slope, linear wave theory predicts that wave  
propagation would be limited, waves would break and, through this process, mixing in the BBL would be enhanced. The  
210 reason for such fundamental differences between theoretical predictions, observations and model outcomes can be understood  
considering the smoothing of the topography that is required by models, even when configured at a resolution high enough to  
permit submesoscale dynamics. Indeed, although the GIGATL simulations provide a reasonable representation of the small-  
scale topographic variability - GIGATL1 more so than GIGATL3 -, the topography remains too smooth to efficiently block and  
contract scattered internal tides.

215 We can verify it by considering the moments of the topographic height spectrum  $H(k)$ . The  $n^{\text{th}}$  moment can be represented  
as

$$\int_0^{\infty} k^n H(k) dk \quad (6)$$

For abyssal hills,  $H(k)$  is commonly fractal, i.e. for high horizontal wavenumbers,  $H(k) \propto k^{-x}$  with  $2 < x < 3$ , see also  
Fig. 5.



**Table 1.** Moments of the topographic spectrum  $H(k)$ , Eq. 6 and (7). We find that the second moment is of similar magnitude as the square of the semi-diurnal ray trajectory slope, with  $N=1 \times 10^{-3} \text{s}^{-1}$ . See Polzin (2004, 2009) for further discussion of the dimensions and  $O(1)$  pre-factors.

$n =$	0	1	2	4
multibeam bathymetry ( $mb$ )	1.9314e+04 [ $\text{m}^2$ ]	14 [m]	0.024 [ $\text{m}^{-1}$ ]	3.3e-07 [ $\text{m}^{-2}$ ]
$\frac{srtm}{mb}$	0.86	0.62	0.32	0.050
$\frac{1km}{mb}$	0.50	0.22	0.061	1.8e-3
$\frac{3km}{mb}$	0.11	0.19	1.9e-3	7.8e-06

220 The implication is that the integral for the first moment converges, but not the second, or fourth. Linear wave kinematics prescribes a rate of energy transfer from the barotropic to baroclinic tide (generation) proportional to the first moment, while the energy density of the internal tide is proportional to the second moment and the shear variance, which relates to wave-breaking, is proportional to the fourth moment. Finescale parameterizations then connect turbulent dissipation to the square of this fourth moment. A prediction of infinite second moment implies infinite energy density, which is of course unfounded, and theoretically is avoided by using a quasi-linear model of wave generation which places the linear analysis in the advected coordinate of the barotropic tide. This effectively regularizes the integrals defining the moments (Eq. 6) by introducing an integration endpoint of approximately  $k_{cut} = \lambda_h = 4U_0/\sigma$ , where  $U_0$  represents the velocity amplitude of the barotropic tide and  $\sigma$  its frequency.  $\lambda_h$  is about 1 km in the Brazil Basin, significantly smaller than the 6-8 km distance between hill crests, and a velocity amplitude of  $U_0=0.03 \text{ m s}^{-1}$  maps well onto a peak in the observed near-bottom vertical wavenumber shear spectrum.

230 Table 1 compares the moments associated with four data sets of the Brazil Basin bathymetry using a normalized spectral moment truncated at  $k_{cut}$ :

$$\frac{\int_0^{k_{cut}} k^n H_{mb}(k) dk}{\int_0^{k_{cut}} k^n H_{...}(k) dk} \tag{7}$$

We considered multibeam data from nearby the tracer injection site in the Brazil Basin shown in Fig. 5a and the topographic height spectral density  $H_{mb}(k)$  shown in Fig. 5b, the SRTM\_30 plus product  $H_{srtm}(k)$ , the GIGATL1 bathymetry  $H_{1km}(k)$ , and the GIGATL3 bathymetry  $H_{3km}(k)$ .  $k_{cut}$  is set to be equal to the Nyquist wavenumber of the SRTM and model products. The results summarized in table 1 imply an energy transfer from barotropic to baroclinic tides. Even in the higher resolution GIGATL1 case, there is nearly an order of magnitude difference in the second moment (energetics) and an even greater underestimation for the model fourth moment (shear variance). Our interpretation is that the smoothing of the bathymetry in the GIGATL1 (GIGATL3) runs, and more generally in ocean models, generates reliefs that retain the key features at scales larger than  $3 - 4 \times 10 \text{ km}$  but removes small-scale roughness, allowing isopycnal spreading over the ridge and an appreciable velocity



curvature  $U_{zz}$ . The resulting flow facilitates baroclinic and submesoscale instabilities which convert available potential energy into eddy kinetic energy, supporting the generation of strong eddies. Rough topography in the real ocean, on the other hand, converts geostrophic flow into internal lee waves that remove energy from the eddy field and feed small scale shear and mixing. With a smoothed topography CROCO generates less of these waves than the real ocean, the eddy field loses a principal energy sink and the result is a more energetic flow field. Eddies persist at higher amplitude and contribute to an elevated K that extends to the ocean interior, and to an overall barotropization of the water column, as done near the surface as well (Yankovsky et al., 2022).

The key differences in bottom roughness between model and observations can be further assessed looking at the differences in the vertical wavenumber spectra. The vertical KE spectra for the deep Brazil Basin in the GIGATL1 runs and in the observations are compared in Fig. 5cd. The model captures the observed near-inertial peak. In horizontal wavenumber space, the modeled and observed spectra agree reasonably well at low wavenumbers, yet the energy in CROCO decays too fast at high wavenumber. The model vertical wavenumber bandwidth (i.e.  $j_*$ ) is also slightly smaller than the observations, speaking to the impacts of CROCO finite spatial resolution, which, in combination with the smoothed topography, acts on the representation of the generation and scattering processes. The more rapid spectral roll-off compared to observations suggests an inefficient forward cascade of energy to fine scales in the simulation. Indeed, the model retains much of its energy in long-lived, coherent mesoscale eddies.

The vertical wavenumber spectra for both the model and the observational data document relatively low KE to PE ratios at the largest resolved vertical wavelengths, increasing at 500 m wavelength. We interpret such increasing ratios as a result of parametric subharmonic instability transfers from the semi-diurnal internal tide to near-inertial waves. The model near-inertial field, however, is less developed than in the observations. At subinertial frequencies, the model spectra indicate decidedly greater eddy variability at periods of 10 days, which we attribute to the submesoscale field. The field record extends to nearly two years and documents the presence of longer periods that we cannot presently assess.

Again, this analysis supports the hypothesis that the simulation lacks the high wavenumber internal tides because of the smoothed bathymetry. The attenuation of the background internal wave spectrum at high vertical wavenumber and other (both higher and lower) frequencies in turn precludes the damping of the mesoscale circulations that grow more numerous and intense in the submesoscale permitting case.

## 5 Conclusions

The genesis of enhanced turbulent mixing above rough topography has been discussed extensively in recent decades (Polzin and McDougall, 2022). Given the role that diapycnal mixing plays in shaping the distribution of heat and carbon and the overall overturning circulation, it is paramount to capture its variability in time and space. Observations remain limited and model simulations are strongly constrained by resolution, vertical discretization choices, approximations adopted (most commonly the hydrostatic assumption) and parameterization schemes implemented, or, in the case of direct numerical simulations, size and realism of the integration domains. The contribution of each dynamical process involved with diapycnal mixing in the

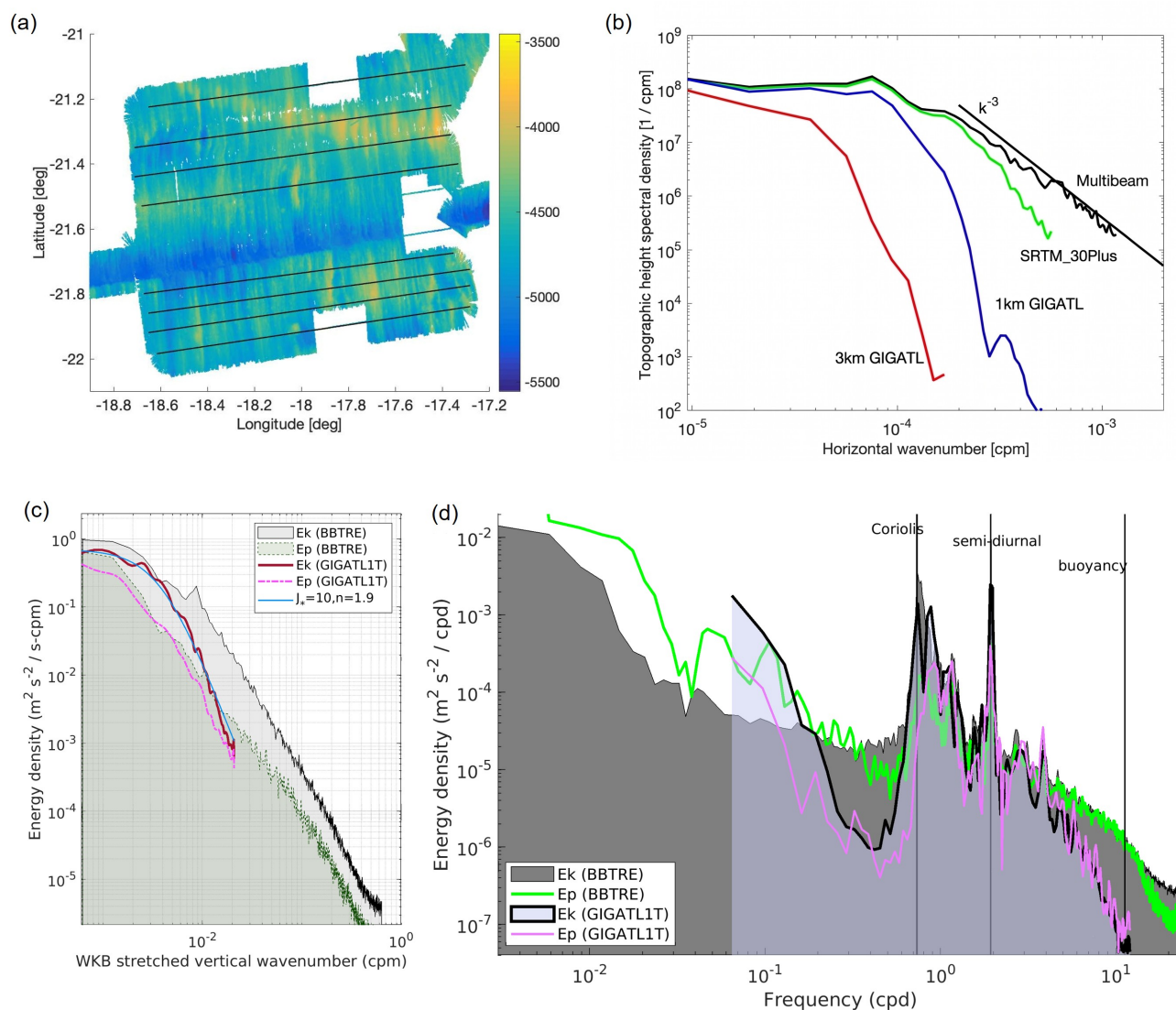


**Figure 5.** (a) multi-beam topography from the vicinity of the BBTRE tracer injection site. Ping data were mapped onto a 50 m grid and this map was used to create estimates of bathymetry vs distance along the indicated lines. (b) Estimates of bathymetry from the SRTM\_30plus data set and the GIGATL grids were interpolated onto the multi-beam product coordinates. All datasets were Fourier transformed to quantify the impact of filtering in the three derivative representations. (c) Stretched vertical wavenumber spectra Wentzel-Kramer-Brillouin (WKB) approximation of horizontal kinetic (Ek) and potential energy (Ep). The blue line represents a fit of the GM (Garrett–Munk) model:  $1/((j_*^2 + j^2)^n$ , which provides an estimate of the background internal-wave energy under approximate horizontal isotropy and scaling with local stratification, while  $j$  represents the vertical wavenumber with the scale height of 1300 m. (d) Horizontal kinetic energy and potential energy frequency spectra at BBTRE site at 3000 m.



275 BBL remains unconstrained, especially in regions characterized by very rough topography. This is the case of the Brazil Basin, where topographic features are of order  $O(1)$  km.

Diapycnal mixing in the deep Brazil Basin is known to be significantly elevated over rough bathymetry and decline when moving into the ocean interior (Polzin et al., 1997). The simulations considered here - at 1 km and 3 km horizontal resolution, with and without tide, reproduce this trend:  $K$  peaks near the bottom and declines with height, and in the BBL is broadly  
280 consistent in magnitude with that observed during the BBTRE campaign. However, modeled diffusivities are overestimated in the ocean interior. This discrepancy suggests that CROCO fails to suppress excessive mixing in the stratified interior, and mesoscale eddies emerge as critical in the abyssal Brazil Basin. The instabilities that occur over rough topography as represented by the model facilitate the generation of eddies that extend from the BBL into the water column, displacing isopycnals. Localized increased vertical mixing is found around and within these eddies, which are stronger and more numerous in the  
285 GIGATL1 simulations because that the scale of the instabilities responsible for their generation is better resolved. As a result, GIGATL1 runs overestimate the observed vertical diffusivities more so than the GIGATL3 counterparts. At the same time, the model underestimates the high-wavenumber energy because the smoothed topography precludes a realistic internal wave generation. In summary, two non-exclusive processes explain the eddy–wave partitioning in the model simulations: on one hand, buoyancy anomalies favorable to baroclinic instability are amplified relative to reality; on the other, the absence of a realistic  
290 internal-wave field removes an energy sink that would otherwise damp eddies.

As note of caution, we stress that beyond eddy dynamics, vertical mixing parameterizations and the numerical schemes employed also contributes to the biased interior diffusivity. The GIGATL runs employ the  $k^{\sim}\varepsilon$  parameterization. Compared to the widely used KPP (Large et al., 1994) parameterization, the  $k^{\sim}\varepsilon$  one is more sensitive to background settings and to the imposed vertical–mixing value (Warner et al., 2005), which in our runs attains a minimum value of Turbulence Kinetic Energy  
295 (TKE) ( $tke_{min} = 10^{-6}$ ).

In closing, the comparisons among the four simulations and the observations highlight that in mesoscale resolving/submesoscale permitting ocean models, horizontal resolution modulates vertical diapycnal diffusivity and mixing more than tidal forcing. Even at 1 km, the smoothing applied to the bathymetry removes high-wavenumber roughness and the high-mode internal-tide shear and the consequent wave-breaking contributions are underestimated, causing the energy to remain concentrated inside the eddies, which are likely more numerous and intense than in the real ocean. The outcome is that over rough  
300 topography increasing model resolution to a submesoscale permitting regime produces unrealistic, overestimated diffusivities in the ocean interior, and, counterintuitively, more so than in simulations that cannot fully resolve the instabilities responsible for the eddy generation.

In summary, in the case of ocean diapycnal mixing, resolution alone is not the answer, and further research is needed to  
305 improve the realism of traditional ocean models and of the emerging machine-learning based ocean emulators, often trained on submesoscale permitting runs. Furthermore, nonhydrostatic model simulations are needed to advance our understanding of the interactions between internal waves, rough topography, submesoscale instabilities and their impact on the diapycnal mixing and buoyancy transformations in and above the BBL. Moving forward, observational constraints are required to establish how often and by how much the relative contributions of the eddy versus internal wave fields in the BBL are misrepresented in state-

<https://doi.org/10.5194/egusphere-2026-2869>

Preprint. Discussion started: 2 June 2026

© Author(s) 2026. CC BY 4.0 License.



310 of-the-art ocean models. These constraints would also allow to better validate the residence time of heat and carbon across the water column.



## Appendix A: Additional Figures

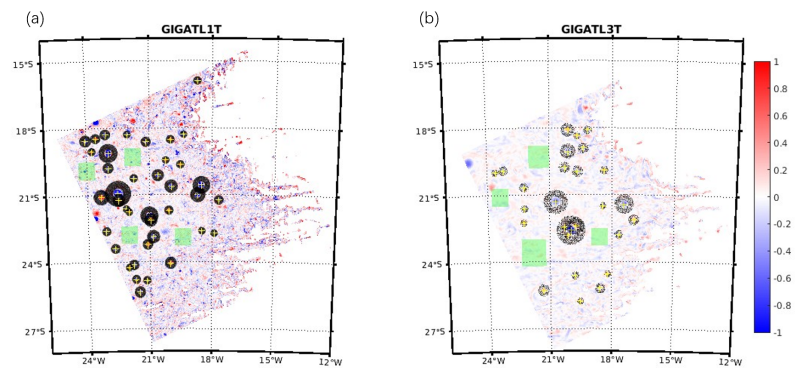


**Figure A1.** Particle release locations in the GIGATL1T (a) and GIGATL3T (b) simulations at 4000 m depth. Relative vorticity is shown in color in the background. Yellow crosses mark the centers of detected eddies. Black circular regions indicate particle releases surrounding coherent eddies, while green boxes indicate releases in background-flow regions without detected eddies.

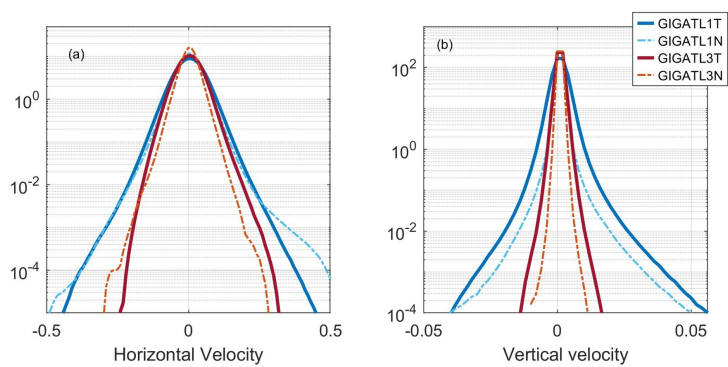


**Figure A2.** The probability density functions of (a) horizontal velocity in  $\text{m s}^{-1}$ , (b) vertical velocity at the top of BBL in  $\text{m s}^{-1}$ .

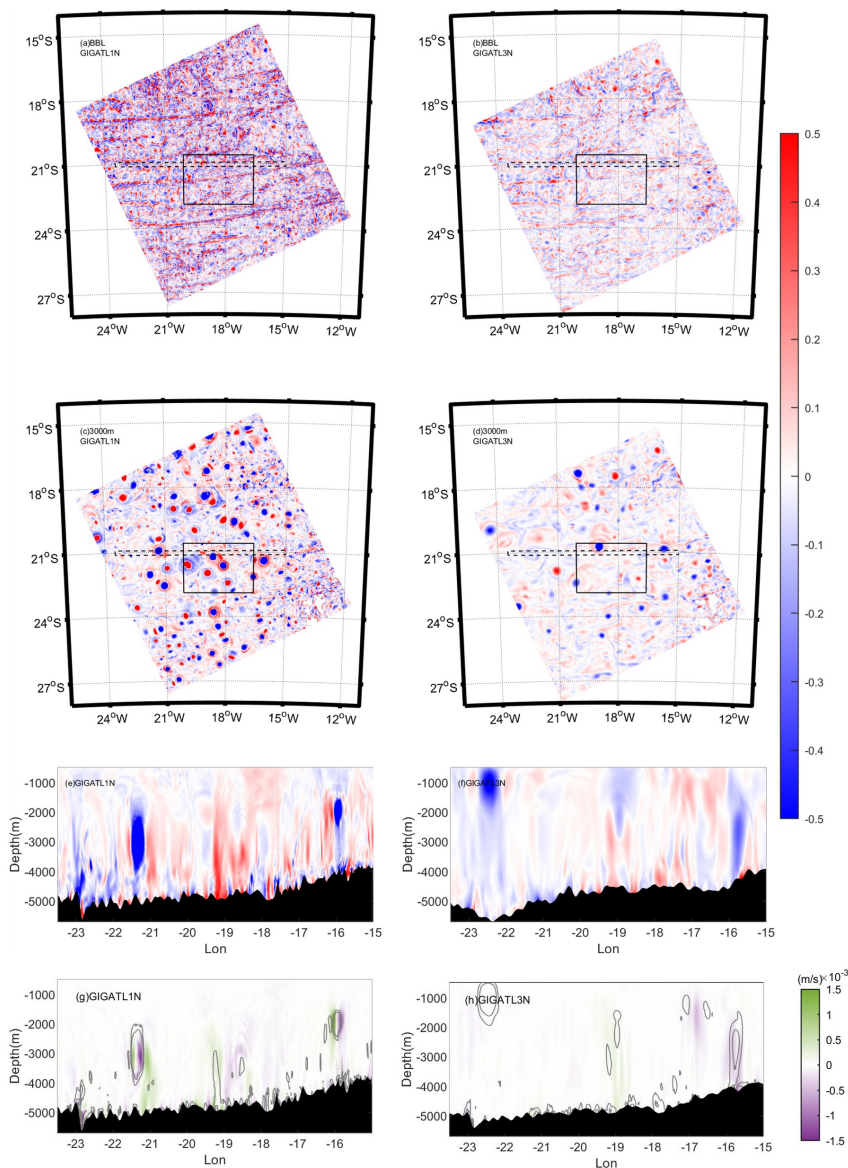


**Figure A3.** A 5-day averaged vorticity field of GIGATL1N (a,c), GIGATL3N (b,d) at 3000 m and at the top of BBL; vorticity profiles along 21°S (dash square in a-d) in the GIGATL1N (e) and GIGATL3N (f) simulations. Vertical velocity slices of GIGATL1N (g) and GIGATL3N (h). Contour lines represent vertical vorticity normalized by the Coriolis parameter ( $\zeta/f$ ), with specified levels at -0.5, -0.25, 0.25, and 0.5 in the GIGATL1N cases (g), and at -0.25, -0.125, 0.125, and 0.25 in the GIGATL3N simulations (h).

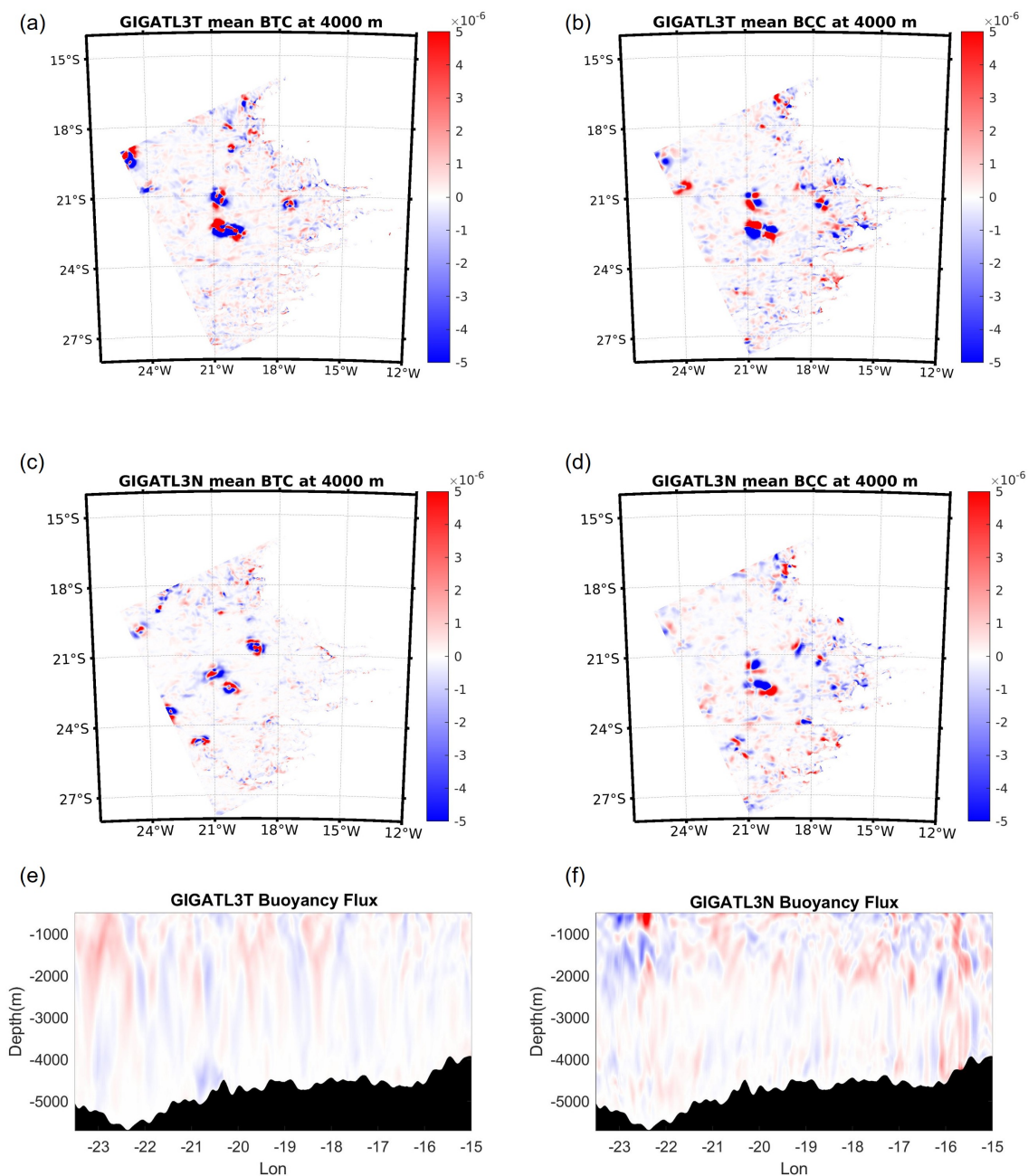


**Figure A4.** Monthly mean of BTC (a,c) and BCC (b,d) at the depth of 4000m in GIGATL3T and GIGATL3N. Profiles of 5-days averaged buoyancy flux along 21°S in (e) GIGATL3T and (f) GIGATL3N.

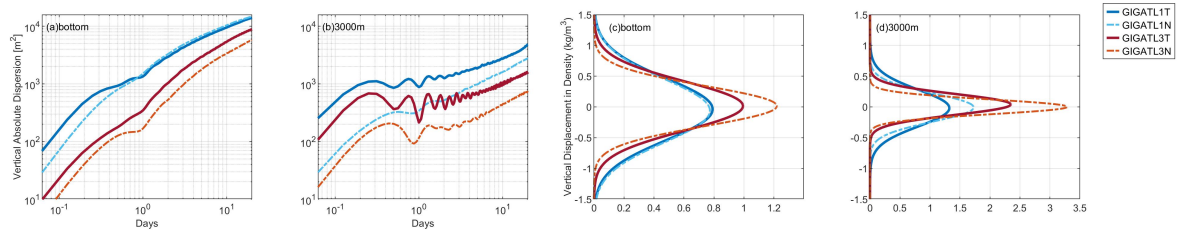


**Figure A5.** Vertical absolute dispersion (m) (a-b); Vertical diapycnal displacement of tracer particles at Day 20 after release (c-d)



315 *Data availability.* Data analyzed in this study are currently stored on the TGCC supercomputing center and/or at the Datarmor supercomputing center at Ifremer in Plouzané, France. Regional extractions are available upon request ([gula@univ-brest.fr](mailto:gula@univ-brest.fr))

*Author contributions.* Yonglin Huang: Conceptualization, Methodology, Investigation, Writing - Original Draft, Visualization; Annalisa Bracco: Conceptualization, Writing - Review and Editing, Supervision, Funding acquisition; Kurt Polzin: Review and Editing, Project administration; Jonanthan Gula: Data Curation

*Competing interests.* The authors declare that they have no conflict of interest.

320 *Acknowledgements.* We acknowledge the support of the National Science Foundation under Grant Numbers OCE-2232440 (Y.H. and A.B.) and OCE-2232439 (K.P.). Data analyzed in this study are currently stored on the TGCC supercomputing center and/or at the Datarmor supercomputing center at Ifremer in Plouzané, France. Regional extractions are available upon request ([gula@univ-brest.fr](mailto:gula@univ-brest.fr))



## References

- Auclair, F. et al.: Coastal and Regional Ocean COMMunity model, <https://doi.org/10.5281/zenodo.7415055>, 2024.
- 325 Bracco, A., Choi, J., Joshi, K., Luo, H., and McWilliams, J. C.: Submesoscale currents in the northern Gulf of Mexico: Deep phenomena and dispersion over the continental slope, *Ocean Modelling*, 101, 43–58, <https://doi.org/10.1016/j.ocemod.2016.03.002>, 2016.
- Brum, A. L., Azevedo, J. L. L. d., and Dengler, M.: Energetics of eddy–mean flow interactions in the deep western boundary current off the northeastern coast of Brazil, *Deep Sea Research Part I: Oceanographic Research Papers*, 193, 103 965, <https://doi.org/10.1016/j.dsr.2023.103965>, 2023.
- 330 Callies, J.: Restratification of abyssal mixing layers by submesoscale baroclinic eddies, *Journal of Physical Oceanography*, 48, 1995–2010, <https://doi.org/10.1175/JPO-D-18-0082.1>, 2018.
- Carton, J. A. and Giese, B. S.: A Reanalysis of Ocean Climate Using Simple Ocean Data Assimilation (SODA), *Monthly Weather Review*, 136, 2999–3017, <https://doi.org/10.1175/2007MWR1978.1>, 2008.
- Chen, Z., Wenegrat, J., Chor, T., and Marchesiello, P.: Evaluating Turbulence Parameterizations at Gray Zone Resolutions for the Ocean Surface Boundary Layer, *Journal of Advances in Modeling Earth Systems*, 17, e2025MS005 104, <https://doi.org/10.1029/2025MS005104>, 2025.
- 335 Dheeshjith, S., Subel, A., Adcroft, A., Busecke, J., Fernandez-Granda, C., Gupta, S., and Zanna, L.: Samudra: An AI Global Ocean Emulator for Climate, *Geophysical Research Letters*, 52, e2024GL114 318, <https://doi.org/10.1029/2024GL114318>, 2025.
- Drake, H. F., Ruan, X., Callies, J., Ogden, K., Thurnherr, A. M., and Ferrari, R.: Dynamics of Eddying Abyssal Mixing Layers over Sloping Rough Topography, *Journal of Physical Oceanography*, 52, 3199–3219, <https://doi.org/10.1175/JPO-D-22-0009.1>, 2022a.
- 340 Drake, H. F., Ruan, X., and Ferrari, R.: Diapycnal Displacement, Diffusion, and Distortion of Tracers in the Ocean, *Journal of Physical Oceanography*, 52, 3221–3240, <https://doi.org/10.1175/JPO-D-22-0010.1>, 2022b.
- Ferrari, R., Mashayek, A., McDougall, T. J., Nikurashin, M., and Campin, J.-M.: Turning Ocean Mixing Upside Down, *Journal of Physical Oceanography*, 46, 2239–2261, <https://doi.org/10.1175/JPO-D-15-0244.1>, 2016.
- 345 Garrett, C., MacCready, P., and Rhines, P.: Boundary mixing and arrested Ekman layers: Rotating stratified flow near a sloping boundary, *Annual Review of Fluid Mechanics*, 25, 291–323, <https://doi.org/10.1146/annurev.fl.25.010193.001451>, 1993.
- Gula, J., Theetten, S., Cambon, G., and Roullet, G.: Description of the GIGATL simulations, <https://doi.org/10.5281/zenodo.4948523>, 2021.
- Large, W. G., McWilliams, J. C., and Doney, S. C.: Oceanic vertical mixing: A review and a model with a nonlocal boundary layer parameterization, *Reviews of Geophysics*, 32, 363–403, <https://doi.org/10.1029/94RG01872>, 1994.
- 350 Ledwell, J. R.: The Brazil Basin Tracer Release Experiment: Observations, *Journal of Physical Oceanography*, 54, 1105–1120, <https://doi.org/10.1175/JPO-D-22-0249.1>, 2024.
- Ledwell, J. R., Montgomery, E. T., Polzin, K. L., St. Laurent, L. C., Schmitt, R. W., and Toole, J. M.: Evidence for enhanced mixing over rough topography in the abyssal ocean, *Nature*, 403, 179–182, <https://doi.org/10.1038/35003164>, 2000.
- Ledwell, J. R., He, R., Xue, Z., DiMarco, S. F., Spencer, L., and Chapman, P.: Dispersion of a tracer in the deep Gulf of Mexico, *Journal of Geophysical Research: Oceans*, 121, 1110–1132, <https://doi.org/10.1002/2015JC011405>, 2016.
- 355 Legg, S. and Klymak, J.: Internal Hydraulic Jumps and Overturning Generated by Tidal Flow over a Tall Steep Ridge, *Journal of Physical Oceanography*, 38, 1949–1964, <https://doi.org/10.1175/2008JPO3777.1>, 2008.



- Mashayek, A., Gula, J., Baker, L. E., Naveira Garabato, A. C., Cimoli, L., Riley, J. J., and de Lavergne, C.: On the role of seamounts in upwelling deep-ocean waters through turbulent mixing, *Proceedings of the National Academy of Sciences of the United States of America*, 121, <https://doi.org/10.1073/pnas.2322163121>, 2024.
- McWilliams, J. C.: Submesoscale currents in the ocean, *Proceedings of the Royal Society A: Mathematical, Physical and Engineering Sciences*, 472, <https://doi.org/10.1098/rspa.2016.0117>, 2016.
- Munk, W. and Wunsch, C.: Abyssal recipes II: Energetics of tidal and wind mixing, *Deep-Sea Research Part I: Oceanographic Research Papers*, 45, 1977–2010, [https://doi.org/10.1016/S0967-0637\(98\)00070-3](https://doi.org/10.1016/S0967-0637(98)00070-3), 1998.
- NASA Shuttle Radar Topography Mission: Shuttle Radar Topography Mission (SRTM) Global, <https://doi.org/10.5069/G9445JDF>, accessed: 2026-05-18, 2013.
- Polzin, K.: Idealized solutions for the energy balance of the finescale internal wave field, *Journal of Physical Oceanography*, 34, 231–246, [https://doi.org/10.1175/1520-0485\(2004\)034<0231:ISFTEB>2.0.CO;2](https://doi.org/10.1175/1520-0485(2004)034<0231:ISFTEB>2.0.CO;2), 2004.
- Polzin, K. L.: An abyssal recipe, *Ocean Modelling*, 30, 298–309, <https://doi.org/10.1016/j.ocemod.2009.07.006>, 2009.
- Polzin, K. L. and McDougall, T. J.: Mixing at the ocean’s bottom boundary, in: *Ocean Mixing: Drivers, Mechanisms and Impacts*, pp. 145–180, <https://doi.org/10.1016/B978-0-12-821512-8.00014-1>, 2022.
- Polzin, K. L., Toole, J. M., Ledwell, J. R., and Schmitt, R. W.: Spatial variability of turbulent mixing in the abyssal ocean, *Science*, 276, 93–96, <https://doi.org/10.1126/science.276.5309.93>, 1997.
- Qu, L., Thomas, L., and Gula, J.: Bottom Mixing Enhanced by Tropical Storm-Generated Near-Inertial Waves Entering Critical Layers in the Straits of Florida, *Geophysical Research Letters*, 48, <https://doi.org/10.1029/2021GL093773>, 2021.
- Ray, R. D.: A Global Ocean Tide Model From TOPEX/POSEIDON Altimetry: GOT99.2, Tech. Rep. NASA Technical Memorandum 209478, NASA Goddard Space Flight Center, 1999.
- Ruan, X. and Ferrari, R.: Diagnosing diapycnal mixing from passive tracers, *Journal of Physical Oceanography*, 51, 757–767, <https://doi.org/10.1175/JPO-D-20-0194.1>, 2021.
- Saha, S. et al.: The NCEP Climate Forecast System Reanalysis, *Bulletin of the American Meteorological Society*, 91, 1015–1058, <https://doi.org/10.1175/2010BAMS3001.1>, 2010.
- Schubert, R., Gula, J., Capó, E., Damien, P., Molemaker, M. J., Vic, C., and McWilliams, J. C.: The ocean flows downhill near the seafloor and recirculates upward above, *Nature Communications*, 16, 5873, <https://doi.org/10.1038/s41467-025-61027-2>, 2025.
- Shchepetkin, A. F. and McWilliams, J. C.: The regional oceanic modeling system (ROMS): a split-explicit, free-surface, topography-following-coordinate oceanic model, *Ocean Modelling*, 9, 347–404, <https://doi.org/10.1016/j.ocemod.2004.08.002>, 2005.
- Song, Y. and Haidvogel, D.: A Semi-implicit Ocean Circulation Model Using a Generalized Topography-Following Coordinate System, *Journal of Computational Physics*, 115, 228–244, <https://doi.org/10.1006/jcph.1994.1189>, 1994.
- Tagliabue, A., Lough, A. J. M., Vic, C., Roussenov, V., Gula, J., Lohan, M. C., Resing, J. A., and Williams, R. G.: Mechanisms Driving the Dispersal of Hydrothermal Iron From the Northern Mid Atlantic Ridge, *Geophysical Research Letters*, 49, <https://doi.org/10.1029/2022GL100615>, 2022.
- Umlauf, L. and Burchard, H.: A generic length-scale equation for geophysical turbulence models, *Journal of Marine Research*, 61, 235–265, <https://doi.org/10.1357/002224003322005087>, 2003.
- Vic, C., Hascoët, S., Gula, J., Huck, T., and Maes, C.: Oceanic Mesoscale Cyclones Cluster Surface Lagrangian Material, *Geophysical Research Letters*, 49, e2021GL097488, <https://doi.org/10.1029/2021GL097488>, 2022.



- 395 Warner, J. C., Sherwood, C. R., Arango, H. G., and Signell, R. P.: Performance of four turbulence closure models implemented using a generic length scale method, *Ocean Modelling*, 8, 81–113, <https://doi.org/10.1016/j.ocemod.2003.12.003>, 2005.
- Wunsch, C. and Ferrari, R.: Vertical mixing, energy, and the general circulation of the oceans, *Annual Review of Fluid Mechanics*, 36, 281–314, <https://doi.org/10.1146/annurev.fluid.36.050802.122121>, 2004.
- Yankovsky, E., Zanna, L., and Smith, K. S.: Influences of Mesoscale Ocean Eddies on Flow Vertical Structure in a Resolution-Based Model Hierarchy, *Journal of Advances in Modeling Earth Systems*, 14, e2022MS003 203, <https://doi.org/10.1029/2022MS003203>, 2022.
- 400 Zanna, L. and Bolton, T.: Data-Driven Equation Discovery of Ocean Mesoscale Closures, *Geophysical Research Letters*, 47, e2020GL088 376, <https://doi.org/10.1029/2020GL088376>, 2020.
- Zhong, Y. and Bracco, A.: Submesoscale impacts on horizontal and vertical transport in the Gulf of Mexico, *Journal of Geophysical Research: Oceans*, 118, 5651–5668, <https://doi.org/10.1002/jgrc.20402>, 2013.